

# Observation of spin-splitter torque in collinear antiferromagnetic RuO<sub>2</sub>

Shutaro Karube,<sup>1,2,\*</sup> Takahiro Tanaka,<sup>1</sup> Daichi Sugawara,<sup>1</sup>  
Naohiro Kadoguchi,<sup>1</sup> Makoto Kohda,<sup>1,2,3,4</sup> and Junsaku Nitta<sup>1,2,3</sup>

<sup>1</sup>*Department of Materials Science, Tohoku University, Sendai 980-8579, Japan*

<sup>2</sup>*Center for Spintronics Research Network, Sendai 980-8577, Japan*

<sup>3</sup>*Center for Science and Innovation in Spintronics (Core Research Cluster), Sendai 980-8577, Japan*

<sup>4</sup>*Division for the Establishment of Frontier Sciences of the Organization for Advanced Studies, Sendai 980-8577, Japan*  
(Dated: November 16, 2021)

The spin-splitter effect is theoretically predicted to generate an unconventional spin current with  $x$ - and  $z$ -spin polarization via the spin-split band in antiferromagnets. The generated torque, namely spin-splitter torque, is effective for the manipulation of magnetization in an adjacent magnetic layer without an external magnetic field for spintronic devices such as MRAM. Here, we study the generation of torque in collinear antiferromagnetic RuO<sub>2</sub> with (100), (101), and (001) crystal planes. Next we find all  $x$ -,  $y$ -, and  $z$ -polarized spin currents depending on the Néel vector direction in RuO<sub>2</sub>(101). For RuO<sub>2</sub>(100) and (001), only  $y$ -polarized spin current was present, which is independent of the Néel vector. Using the  $z$ -polarized spin currents, we demonstrate field-free switching of the perpendicular magnetized ferromagnet at room temperature. The spin-splitter torque generated from RuO<sub>2</sub> is verified to be useful for the switching phenomenon and paves the way for a further understanding of the detailed mechanism of the spin-splitter effect and for developing antiferromagnetic spin-orbitronics.

Remarkable breakthroughs in antiferromagnets (AFMs) [1, 2] have been achieved in spintronics regarding exchange bias-induced field-free switching [3–5], magnetic spin Hall effect (MSHE) [6, 7], and antiferromagnetic spin Hall effect (AFM-SHE) [8]. These intriguing phenomena have led to the establishment of antiferromagnetic spin-orbitronics to further manipulate magnetization effectively for spintronic devices because they are free from the restriction of symmetry regarding spin polarization of the generated spin current, like the conventional spin Hall effect (SHE). While the somewhat novel phenomena concerning unconventional spin-orbit torque in AFMs, such as IrMn<sub>3</sub> [7], PtMn<sub>3</sub> [9], and Mn<sub>2</sub>Au [8] using 5d elements, still depend on spin-orbit coupling, it is difficult to uncover the mechanism generating the torque via the magnetic order. Recently, a spin-split band, through the antiferromagnetic order, was theoretically predicted to cause non-trivial torque, such as  $x$ - and  $z$ -polarized damping-like (DL) torque, even without spin-orbit coupling. This is referred to as the spin-splitter effect (SSE) [10]. Although there is theoretical evidence for the SSE, it has not yet been demonstrated. It is worth noting that there are differences in spin current generation among conventional SHE [11–13], AFM-SHE [8], and the SSE [10] (or MSHE [6, 7]). The spin polarization of the spin current from the SHE is strictly aligned to the  $y$ -direction when we apply the electric field along to  $x$ -direction. Whereas for AFM-SHE [8], the spin polarization, for example the  $z$ -polarized component, can be defined by the Néel vector  $\mathbf{n}$  and spin-orbit field  $\mathbf{H}_{\text{SO}}$ , due to local inversion symmetry breaking in the case of Mn<sub>2</sub>Au, as  $\sigma_z \propto \mathbf{n} \times \mathbf{H}_{\text{SO}} \perp \mathbf{n}$ . On the other hand, the polarization of the spin current generated via the SSE is parallel to

the Néel vector, i.e.,  $\sigma_z \parallel \mathbf{n}$ . In this study, we focus on collinear antiferromagnetic RuO<sub>2</sub>, which theoretically is expected to have the SSE [10], in order to reveal the actual physical mechanism. We systematically extract all  $x$ -,  $y$ -, and  $z$ -polarized components of the DL torque in RuO<sub>2</sub>(100), (101), (001). We find the anisotropic DL torque in all of the components and the  $z$ -polarized DL

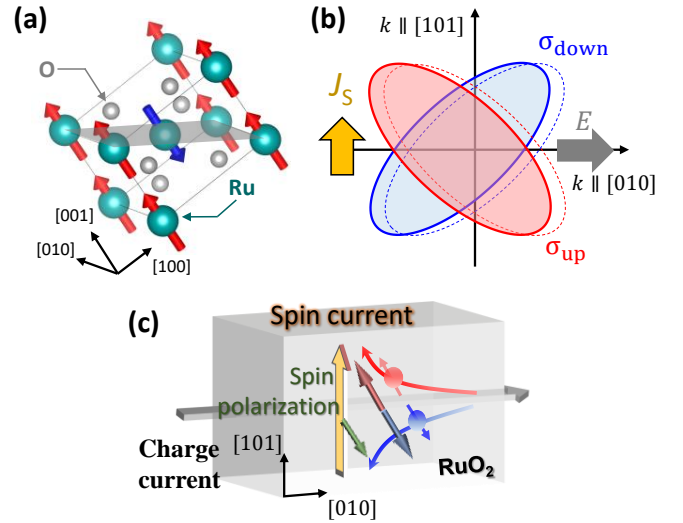


FIG. 1. (a) Crystal structure of RuO<sub>2</sub> with the magnetic moment mostly aligned to [001] or [00 $\bar{1}$ ] on the A and B sites of the Ru atoms. The specific crystal plane using a gray color, corresponds to (101). (b) Spin-split band originating from the RuO<sub>2</sub> antiferromagnetic order at the Fermi level. When we apply the electric field  $E$  along the [010] or [0 $\bar{1}$ 0] direction, the spin current  $J_S$  flowing in the [101] direction can be generated via the spin-splitter effect. (c) Schematic image of spin current generation in RuO<sub>2</sub>(101).

torques, in particular  $\text{RuO}_2(101)$  when applying the charge current along the  $[010]$  direction. Further, using the  $z$ -polarized DL torque, we demonstrate field-free magnetization switching in adjacent magnetic layer.

Ruthenium dioxide ( $\text{RuO}_2$ ) has recently been found to be a collinear antiferromagnet through superexchange coupling between Ru and O ions by means of neutron and X-ray diffraction profiles, which has a rutile-type crystal structure, as shown in Fig. 1(a) (space group:  $P4_2/mnm$ ) [14, 15]. The Néel temperature was over 300 K [14]. The ruthenium oxide is electrically-conductive, which originates from the spin density wave instability at the Fermi surface [14]. The measured conductivity in this study is very similar to those of metals [see Fig. S2 in the Supplemental Material (SM)]. Further, several notable properties regarding the Dirac nodal line (DNL) electronic topology [16], strain-induced superconductivity [17] near 1 K, and crystal Hall effect [18, 19] in strong magnetic fields have been discovered recently. According to the reported diffraction measurements [14, 15], the Néel vector is along  $[001]$  or  $[00\bar{1}]$ , but is not strictly aligned and somewhat canted from this direction. Regarding the magnetic order, the spin current, with the spin polarization aligned to the Néel vector, is driven using a spin-split band structure, as shown in Fig. 1(b). When we apply an electric field to a specific direction, in this case  $[010]$ , spin current flows along  $[101]$ , with not only  $y$ -polarization like conventional SHE, but also  $x$ - and  $z$ -polarization, as shown in Fig. 1(c). This is advantageous for practical magnetization switching without the assistance of a magnetic field.

To elucidate the relationship between the Néel vector and the spin polarization of the generated spin current, we prepared 10 nm-thick  $\text{RuO}_2(100)$ ,  $(101)$ , and  $(001)$ , which have an in-plane, canted, and perpendicular aligned Néel vector, onto  $\text{Al}_2\text{O}_3(0001)$ ,  $\text{Al}_2\text{O}_3(1\bar{1}02)$ , and  $\text{TiO}_2(001)$  single-crystalline substrates respectively, by means of rf magnetron sputtering in an Ar atmosphere (0.24 Pa), introducing partial  $\text{O}_2$  pressure (0.06 Pa). Further the substrate heating was conducted at 400 °C during the deposition. Using X-Ray Diffraction (XRD) and Reflection High Energy Electron Diffraction (RHEED), we evaluated the crystallinity of the deposited films and succeeded in preparing epitaxial films of all the  $\text{RuO}_2$  [see Fig. S1 in the SM]. The longitudinal resistivities  $\rho_{xx}$  of the deposited  $\text{RuO}_2(100)$ ,  $(101)$ , and  $(001)$  are approximately 180  $\mu\Omega\text{cm}$ , 60  $\mu\Omega\text{cm}$ , and 55  $\mu\Omega\text{cm}$ , respectively [see Fig. S2 in the SM]. Further, we deposited 5 nm-thick  $\text{Ni}_{80}\text{Fe}_{20}$  (Py), as a spin detector, and 2 nm-thick  $\text{AlO}_x$ , as a capping layer in-situ. Based on the films, we fabricated rf waveguide devices by means of lift-off process using photolithography and Ar ion milling. First, we employed spin-torque ferromagnetic resonance (ST-FMR) [20, 21] at room temperature (RT), while applying an rf current at 2 dBm and 10 GHz, as shown in Fig. 2(a), to extract the DL torque with  $x$ -,  $y$ - and  $z$ -polarizations,

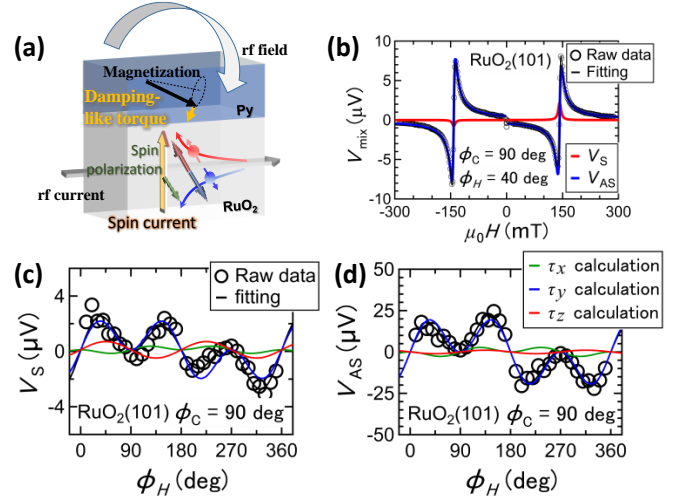


FIG. 2. (a) Schematic image of  $\text{RuO}_2(101)/\text{Py}$  bilayer structure during the ST-FMR measurement. In the resonance field, the magnetization uniformly oscillates due to the rf Oersted field from the  $\text{RuO}_2$  layer, while the spin current is generated via the SSE and injected into the Py layer. (b) ST-FMR raw data as a function of applied in-plane magnetic field. Black plots show the raw data. Black, red, and blue curves indicate fitting and calculations using the analyzed parameters. (c) Symmetric and (d) Antisymmetric voltage amplitudes depending on applied field angle for  $\text{RuO}_2(101)$  in the case where  $\phi_C = 90$  deg. Black plots indicate the extracted values from Fig. 2(b). Black, red, blue, and green curves represent the fitting and calculations of  $\tau_x$ ,  $\tau_y$ , and  $\tau_z$ , respectively, from the analyses using Eqs. (1) and (2).

because this is one of the most reliable techniques for decomposing the three terms [22, 23]. Figure 2(b) shows raw data of the detected ST-FMR signal  $V_{\text{mix}}$  as a function of the applied in-plane magnetic field in the case of  $\text{RuO}_2(101)$ . Here,  $\phi_H$  in Fig. 2(b) corresponds to the angle between the field and the applied current direction.  $\phi_C$  is the angle between the applied current direction and the specific crystal direction ( $[010]$ ,  $[\bar{1}01]$ , and  $[010]$  for  $\text{RuO}_2(100)$ ,  $(101)$ , and  $(001)$ , respectively). The detected signal basically consists of the Lorentzian  $L$  and its derivative,  $V_{\text{mix}} = V_S L(H) + V_{AS} \partial_H L(H)$  [20], where  $V_S$  and  $V_{AS}$  correspond to the amplitudes of the Lorentzian and its derivative, respectively. As shown in Fig. 2(b), the fitting was successfully and decomposed into both the Lorentzian and its derivative. Based on the analysis, we summarized the amplitudes as a function of  $\phi_H$ , as shown in Figs. 2(c) and (d). The  $x$ -,  $y$ - and  $z$ -components can be separated from the  $\phi_H$  dependence using Eqs. (1) and (2) [22, 23].

$$V_S(\phi_H) \propto \sin 2\phi_H [\tau_x^{\text{DL}} \sin \phi_H + \tau_y^{\text{DL}} \cos \phi_H + \tau_z^{\text{FL}}], \quad (1)$$

$$V_{AS}(\phi_H) \propto \sin 2\phi_H [\tau_x^{\text{FL}} \sin \phi_H + \tau_y^{\text{FL}} \cos \phi_H + \tau_z^{\text{DL}}] \quad (2)$$

Here  $\tau_i^{\text{DL}}$  and  $\tau_i^{\text{FL}}$  represent the amplitudes of the DL and field-like (FL) torque, respectively, where subscript  $i$  represents the  $x$ ,  $y$ , and  $z$  components. Through the analyses using Eqs.(1) and (2), the amplitudes were clearly fitted and decomposed into each  $\tau_i^{\text{DL}}$  or  $\tau_i^{\text{FL}}$ . The existences of a NON  $y$ -polarization component is important because this cannot be with the conventional SHE due to the strict orthogonal relationship between the applied charge current, generated spin current, and spin polarization [11–13]. Therefore, this implies that the ST-FMR signal includes both SSE and SHE.

Based on the extracted amplitudes  $V_S$  and  $V_{AS}$ , we estimated the DL torque efficiency per unit electric field using Eqs. (3) and (4) [20].

$$\xi_i^{\text{DL},E} = \frac{\tau_i^{\text{DL}}}{\tau_y^{\text{FL}}} \frac{e\mu_0 M_S t_{\text{Py}} t_{\text{RuO}_2}}{\hbar \rho_{xx}} \sqrt{1 + \frac{\mu_0 M_{\text{eff}}}{\mu_0 H_R}}, \quad (3)$$

$$\xi_z^{\text{DL},E} = \frac{\tau_z^{\text{DL}}}{\tau_y^{\text{FL}}} \frac{e\mu_0 M_S t_{\text{Py}} t_{\text{RuO}_2}}{\hbar \rho_{xx}} \quad (4)$$

Here  $e$ ,  $\mu_0 M_S$ ,  $t_{\text{Py}}$ ,  $t_{\text{RuO}_2}$ ,  $\hbar$ ,  $\rho_{xx}$ ,  $\mu_0 M_{\text{eff}}$ , and  $\mu_0 H_R$  are the elementary charge, saturation magnetization of Py layer, thickness of Py, thickness of RuO<sub>2</sub> layer, the Dirac constant, longitudinal resistivity of RuO<sub>2</sub>, effective magnetization of Py, and Py resonance field at 10 GHz, respectively. Note that  $\sqrt{1 + (\mu_0 M_{\text{eff}}/\mu_0 H_R)}$  is not needed for  $\xi_z^{\text{DL},E}$  in Eq. (4) because both  $\tau_z^{\text{DL}}$  and  $\tau_y^{\text{FL}}$  are from the same antisymmetric voltage  $V_{AS}$ . The effective magnetization  $\mu_0 M_{\text{eff}}$  (0.8 T) was extracted from the Kittel relation in this ST-FMR measurement. The saturation magnetization of the Py layer,  $\mu_0 M_S = 1.1$  T, prepared by us, was extracted from our previous report [24].

The DL torque efficiencies for each component depending on the crystal angle  $\phi_C$  are shown in Fig. 3. These graphs show the relationship of the generated DL torque efficiency between the applied charge current and the Néel vector orientation, as defined above. Regarding RuO<sub>2</sub>(100) and (001), the  $x$ -, and  $z$ -components generated from the SSE are negligible, as shown in Figs. 3 (a), and (c). On the other hand, a finite  $y$ -component of the DL torque efficiency was found and was nearly independent of the crystal angle  $\phi_C$ , i.e. constant the  $\xi_{\text{DL},y}^E$  for RuO<sub>2</sub>(100) and (001) are  $(2.5 \pm 0.2) \times 10^4 [(\hbar/2e) \Omega^{-1} \text{m}^{-1}]$  and  $(6.7 \pm 0.5) \times 10^4 [(\hbar/2e) \Omega^{-1} \text{m}^{-1}]$ , respectively (or  $0.046 \pm 0.003, 0.038 \pm 0.002$  for the dimensionless efficiency  $\xi_{\text{DL},y}$ ). Note that there is a difference in the resistivity between RuO<sub>2</sub> (100) and (001) [see the SM], causing a change in the amplitude relation between  $\xi_{\text{DL},y}^E$  and  $\xi_{\text{DL},y}$ . Remarkably all components of the DL torque efficiency are finite and anisotropic on the crystal angle  $\phi_C$  in the case of RuO<sub>2</sub>(101). The  $x$ -,  $y$ -, and  $z$ -components follow Eqs. (5)-(7), respectively.

$$\xi_{\text{DL},x}^E(\phi_C) = \xi_{\text{SSE},x}^E \sin \phi_C \cos \phi_C \quad (5)$$

$$\xi_{\text{DL},y}^E(\phi_C) = \xi_{\text{SHE},y}^E + \xi_{\text{SSE},y}^E \sin^2 \phi_C \quad (6)$$

$$\xi_{\text{DL},z}^E(\phi_C) = \xi_{\text{SSE},z}^E \sin \phi_C \quad (7)$$

Here  $\xi_{\text{SSE},i}^E$  ( $i = x, y, z$ ) and  $\xi_{\text{SHE},y}^E$  are the amplitudes of the SSE and SHE for each component, respectively. We further investigated a 3 nm-thick Cu insertion case between the RuO<sub>2</sub> and Py layers to exclude the possibility of an exchange bias. We confirmed the same behaviors compared with the case without Cu insertion [see Fig. S3 in the SM].

The anisotropic and independent behaviors regarding the crystal angle  $\phi_C$  for all RuO<sub>2</sub>(100), (101), and (001) could be explained by the orthogonal relation between the applied charge current, spin current, and spin polarization directions. In the SSE, the spin polarization

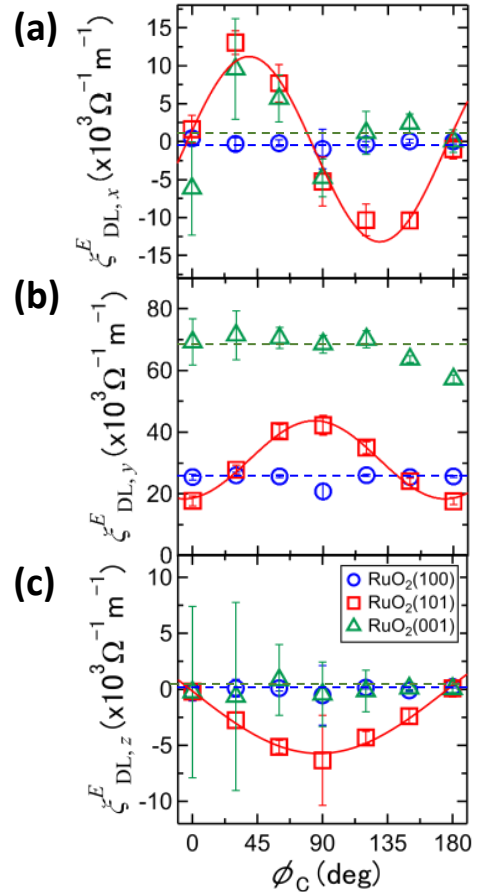


FIG. 3. Damping-like torque efficiency per unit electric field as a function of crystal angle  $\phi_C$  for (a) $x$ -, (b) $y$ -, and (c) $z$ -components. Blue open circle, red open rectangle, and green open triangle correspond to RuO<sub>2</sub>(100), (101), and (001) cases, respectively.

TABLE I. Damping-like torque efficiencies from the spin Hall and spin-splitter effects in RuO<sub>2</sub>(101)

$i$	SSE, $x$	SSE, $y$	SSE, $z$	SHE, $y$
$\xi_i^E [\frac{\hbar}{2e} \Omega^{-1} \text{m}^{-1}]$	$(1.2 \pm 0.1) \times 10^4$	$(2.5 \pm 0.1) \times 10^4$	$-(5.8 \pm 0.5) \times 10^3$	$(1.8 \pm 0.8) \times 10^4$
$\xi_i [-]$	$0.0066 \pm 0.0005$	$0.0138 \pm 0.0001$	$-0.0032 \pm 0.0003$	$0.0099 \pm 0.0044$
$\xi_i/\xi_{\text{SHE},y} [-]$	0.67	1.39	-0.32	-

of the generated spin current follows the Néel vector direction approximately [14, 15]. As for RuO<sub>2</sub>(001) with a perpendicular Néel vector against the film plane, the spin polarization and flowing spin current directions are parallel to each other, thus the spin current can no longer occur. Therefore, we found that only the  $y$ -component of the DL torque generated by the SHE, as shown in Fig.3 (b). Further, in the case of RuO<sub>2</sub>(101) with a canted Néel vector, all components of the torque may appear and should be anisotropic to the Néel vector direction. The possible contribution of spin-orbit precession (SOP) torque [25] generated at the RuO<sub>2</sub>/Py interface has been considered. This torque may have non  $y$ -components of the DL torque due to precessional motion being induced by the Rashba effect at the interface. Note that now the effective field generated by the Rashba effect is always perpendicular to the applied current direction; the SOP should be independent of  $\phi_C$ , therefore, we conclude that the SOP effect is negligible in this RuO<sub>2</sub>/Py bilayer. Regarding RuO<sub>2</sub>(100) with an in-plane Néel vector, the  $z$ -component should not appear, while the  $x$ -component may be generated when the applied current and the Néel vector have relative angles on the in-plane; however, as shown in Fig.3 (a), this was not observed. The possible reason for negligible  $x$ -component spin current in RuO<sub>2</sub>(100) is due to higher scattering rate  $\Gamma$  than that of RuO<sub>2</sub>(101). The SSE is related to the  $\mathcal{T}$ -odd spin Hall conductivity depending on the  $\Gamma$ . The estimated  $\Gamma$  from  $\rho_{xx}$  in RuO<sub>2</sub>(100) is 31 meV, while  $\Gamma$  in RuO<sub>2</sub>(101) is 9.5 meV. The quantitative comparison with the theory [10] is still difficult, but it predicts that the scattering rate suppresses the SSE. Next, we estimated all amplitudes for RuO<sub>2</sub>(101), as shown in TABLE I, based on the angular dependence. The amplitude ratio between the SSE and SHE is larger or comparable for all  $x$ -,  $y$ -, and  $z$ -components. Thus, we have efficiently found finite but small  $x$ -,  $y$ -, and  $z$ -components of the DL torque, even though the theory for the SSE predicted much higher efficiency values, approximately 30 % [10]. This result is attributed to the AFM domain structure [26] cancelling out the unidirectional Néel vector contribution. Although we have found 2-fold in-plane crystal symmetry in RuO<sub>2</sub>(101) [see Fig. S4 in the SM], the two peaks are broad, implying that the prepared RuO<sub>2</sub> is distorted. This could lead to the AFM domain structure reducing the unconventional torque originating from the SSE, because the distortion would make the AFM locally ordered

due to weak superexchange coupling between the Ru and O ions. Further, for the amplitude comparison of the detected  $y$ -components among RuO<sub>2</sub>(100), (101), and (001), we are currently unable to fully understand the relation even when consider the contribution of the expected DNL topology [16]. When the electrons in RuO<sub>2</sub> travel on the (110) and  $(\bar{1}10)$  planes, the Berry curvature driven by the DNL topology occurs, enhancing the  $y$ -component of the DL torque efficiency. In this case, we should see the enhancement of the torque near the (110) and  $(\bar{1}10)$  planes, dependent on the crystal angle  $\phi_C$ .

Next we demonstrated the field-free switching using the  $z$ -polarization component of the DL torque in RuO<sub>2</sub>(101) at RT. For the experiment, we fabricated a RuO<sub>2</sub>(101)(10 nm)/Ru(0.8 nm)/Co(0.8 nm)/Pt(2 nm) multilayer structure, as shown in Fig. 4(a). The roles of the Ru and Pt layers are to break the RuO<sub>2</sub> crystallinity and to introduce a perpendicular magnetic anisotropy (PMA) of the Co layer through hexagonal closed packed structure and spin-orbit coupling. Note that the 2 nm-thick Pt layer would not contribute to the switching of the Co layer through the generated spin-orbit torque because most of the charge current flows into the 10 nm-thick RuO<sub>2</sub>(101) layer due to current shunting. The calculated shunting factors for the Pt and RuO<sub>2</sub>(101) layers are 0.06 and 0.94 [see the SM], respectively, thus, the current dominantly flows into the RuO<sub>2</sub> layer. Furthermore, the spin current generation is not sufficient in the Pt layer due to the comparable thickness of the spin diffusion length ( $\lambda_{\text{sd}}^{\text{Pt}} \approx 1.0$  nm) [27]. As shown in Fig. 4(a), when we apply the charge current along  $[\bar{1}01]$  direction ( $\phi_C = 0$  deg), without the  $z$ -polarization DL torque, switching cannot fully occur even when applying large current (Fig. 4(b)). When the current is applied  $[010]$  direction ( $\phi_C = 90$  deg), with the  $z$ -polarization component, the full switching is observed (Fig. 4(c)); therefore,  $z$ -polarization is necessary for field-free switching. To ensure occurrence of the  $z$ -component, we confirmed an effective perpendicular field  $\mu_0 H_z^{\text{eff}}$  depending on the current amplitude along  $[010]$  direction [see Fig. S5 in SM]. On the other hand, halfway switching, in the case of  $\phi_C = 0$  deg, as shown in Fig. 4(b), would originate from the perpendicular exchange bias. We have only observed the finite exchange bias where  $\phi_C = 0$  deg, whereas it was negligible when  $\phi_C = 90$  deg [see the SM as shown in Fig. S6]. This bias prevents reverse switching due to pinning the magnetization along the bias direction. A finite  $y$ -



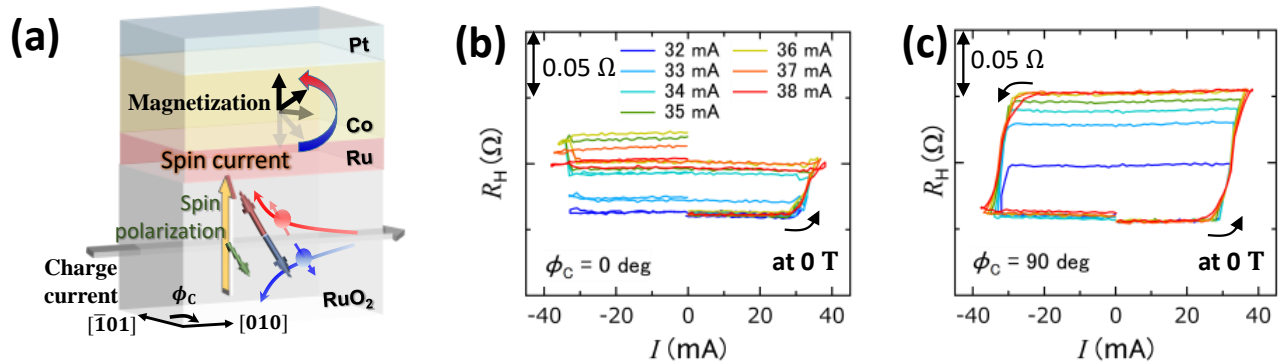


FIG. 4. (a) Schematic illustration of  $\text{RuO}_2(101)(10\text{nm})/\text{Ru}(0.8\text{nm})/\text{Co}(0.8\text{nm})/\text{Pt}(2\text{nm})$  multilayer. The  $z$ -polarized spin current generated via the SSE is injected into the Co layer, then the magnetization is switched without the assisting external magnetic field. Hall resistance of the Co layer when applying the DC current  $I$  for the switching in the case of (b)  $\phi_C = 0$  deg and (c) 90 deg.

component of the DL torque turn the magnetization, but is unable to fully switch it without the  $z$ -component of the DL torque generated via the SSE. In the case where  $\phi_C = 90$  deg, we observed memristive behavior with a change in the current amount. The observed memristive behavior is explained in terms of multi-domain structure in the PMA Co layer induced by exchange coupling between AFM  $\text{RuO}_2$  and ferromagnetic Co layers as is previously reported in a  $\text{PtMn}/[\text{Co}/\text{Ni}]_n$  structure [3]. We emphasize that the demonstration of the field-free switching does not originate from the exchange bias, but the  $z$ -component of the DL torque generated from  $\text{RuO}_2(101)$ . The in-plane exchange bias is induced along the  $[\bar{1}01]$  direction ( $\phi_C = 0$  deg) due to the canted Néel vector. Hereby, we have successfully demonstrated the generation of spin-splitter torque, including all  $x$ -,  $y$ -, and  $z$ -components of the DL torque and the field-free switching driven by the unconventional torque.

In summary, we prepared collinear antiferromagnetic  $\text{RuO}_2(100)$ ,  $(101)$ , and  $(001)$  grown epitaxially, where the SSE is theoretically expected to generate the unconventional DL torque [10]. Using the epitaxial films, all  $x$ -,  $y$ -, and  $z$ -components of the DL torque in the ruthenium oxides have been systematically investigated by means of the ST-FMR technique. Interestingly, the finite unconventional  $x$ - and  $z$ -components of the DL torque, depending on the Néel vector direction, have been observed in  $\text{RuO}_2(101)$ . These components clearly originate from the SSE. Using the  $z$ -component of the DL torque from  $\text{RuO}_2$ , we have demonstrated field-free switching in the FM layer with the PMA. So, this study provides a novel spin current generation and a technique to manipulate the spins effectively for antiferromagnetic spin-orbitronics.

We would like to thank Prof. Akimasa Sakuma, Dr. Chaoliang Zhang, and Yuta Yahagi for constructive discussions. Further, this work is partially supported by

the Japan Society for the Promotion of Science (JSPS) (Grants No. 15H05699, and No. 18K14111), the Center for Spintronics Research Network at Tohoku University, and the Center for Science and Innovation in Spintronics at Tohoku University.

\* karube@material.tohoku.ac.jp

- [1] V. Baltz, A. Manchon, M. Tsoi, T. Moriyama, T. Ono, and Y. Tserkovnyak, *Rev. Mod. Phys.* **90**, 015005 (2018).
- [2] A. Manchon, J. Železný, I. M. Miron, T. Jungwirth, J. Sinova, A. Thiaville, K. Garello, and P. Gambardella, *Rev. Mod. Phys.* **91**, 035004 (2019).
- [3] S. Fukami, C. Zhang, S. DuttaGupta, A. Kurenkov, and H. Ohno, *Nat. Mater.* **15**, 535 (2016).
- [4] Y.-W. Oh, S.-H. C. Baek, Y. M. Kim, H. Y. Lee, K.-D. Lee, C.-G. Yang, E.-S. Park, K.-S. Lee, K.-W. Kim, G. Go, J.-R. Jeong, B.-C. Min, H.-W. Lee, K.-J. Lee, and B.-G. Park, *Nat. Nanotechnol.* **11**, 878 (2016).
- [5] Y.-C. Lau, D. Betto, K. Rode, J. M. D. Coey, and P. Stamenov, *Nat. Nanotechnol.* **11**, 758 (2016).
- [6] M. Kimata, H. Chen, K. Kondou, S. Sugimoto, P. K. Muduli, M. Ikhlas, Y. Omori, T. Tomita, A. H. MacDonald, S. Nakatsuji, and Y. Otani, *Nature* **565**, 627 (2019).
- [7] J. Holanda, H. Saglam, V. Karakas, Z. Zang, Y. Li, R. Divan, Y. Liu, O. Ozatay, V. Novosad, J. E. Pearson, and A. Hoffmann, *Phys. Rev. Lett.* **124**, 087204 (2020).
- [8] X. Chen, S. Shi, G. Shi, X. Fan, C. Song, X. Zhou, H. Bai, L. Liao, Y. Zhou, H. Zhang, A. Li, Y. Chen, X. Han, S. Jiang, Z. Zhu, H. Wu, X. Wang, D. Xue, H. Yang, and F. Pan, *Nat. Mater.* **20**, 800 (2021).
- [9] H. Bai, X. F. Zhou, H. W. Zhang, W. W. Kong, L. Y. Liao, X. Y. Feng, X. Z. Chen, Y. F. You, Y. J. Zhou, L. Han, W. X. Zhu, F. Pan, X. L. Fan, and C. Song, *Phys. Rev. B* **104**, 104401 (2021).
- [10] R. González-Hernández, L. Šmejkal, K. Výborný, Y. Yahagi, J. Sinova, T. Jungwirth, and J. Železný, *Phys. Rev. Lett.* **126**, 127701 (2021).
- [11] M. I. Dyakonov and V. I. Perel, *JETP Letters* **13**, 467

- (1971).
- [12] T. Kimura, Y. Otani, T. Sato, S. Takahashi, and S. Maekawa, *Phys. Rev. Lett.* **98**, 156601 (2007).
  - [13] E. Saitoh, M. Ueda, H. Miyajima, and G. Tatara, *Appl. Phys. Lett.* **88**, 182509 (2006).
  - [14] T. Berlijn, P. C. Snijders, O. Delaire, H.-D. Zhou, T. A. Maier, H.-B. Cao, S.-X. Chi, M. Matsuda, Y. Wang, M. R. Koehler, P. R. C. Kent, and H. H. Weiering, *Phys. Rev. Lett.* **118**, 077201 (2017).
  - [15] Z. H. Zhu, J. Strempler, R. R. Rao, C. A. Occhialini, J. Pellicari, Y. Choi, T. Kawaguchi, H. You, J. F. Mitchell, Y. Shao-Horn, and R. Comin, *Phys. Rev. Lett.* **122**, 017202 (2019).
  - [16] V. Jovic, R. J. Koch, S. K. Panda, H. Berger, P. Bugnon, A. Magrez, K. E. Smith, S. Biermann, C. Jozwiak, A. Bostwick, E. Rotenberg, and S. Moser, *Phys. Rev. B* **98**, 241101(R) (2018).
  - [17] M. Uchida, T. Nomoto, M. Musashi, R. Arita, and M. Kawasaki, *Phys. Rev. Lett.* **125**, 147001 (2020).
  - [18] L. Šmejkal, R. González-Hernández, T. Jungwirth, and J. Sinova, *Sci. Adv.* **6**, eaaz8809 (2020).
  - [19] Z. Feng, X. Zhou, L. Šmejkal, L. Wu, Z. Zhu, H. Guo, R. González-Hernández, X. Wang, H. Yan, P. Qin, X. Zhang, H. Wu, H. Chen, Z. Xia, C. Jiang, M. Coey, J. Sinova, T. Jungwirth, and Z. Liu, *arXiv*, 2002.08712 (2021).
  - [20] L. Liu, T. Moriyama, D. C. Ralph, and R. A. Buhrman, *Phys. Rev. Lett.* **106**, 036601 (2011).
  - [21] D. Fang, H. Kurebayashi, J. Wunderlich, K. Výborný, L. P. Žárbo, R. P. Campion, A. Casiraghi, B. L. Gallagher, T. Jungwirth, and A. J. Ferguson, *Nat. Nanotechnol.* **6**, 413 (2011).
  - [22] T. Nan, C. X. Quintela, J. Irwin, G. Gurung, D. F. Shao, J. Gibbons, N. Campbell, K. Song, S. Y. Choi, L. Guo, R. D. Johnson, P. Manuel, R. V. Chopdekar, I. Hallstein, T. Tybell, P. J. Ryan, J. W. Kim, Y. Choi, P. G. Radaelli, D. C. Ralph, E. Y. Tsymbal, M. S. Rzchowski, and C. B. Eom, *Nat. Commun.* **11**, 4671 (2020).
  - [23] D. MacNeill, G. M. Stiehl, M. H. D. Guimaraes, R. A. Buhrman, J. Park, and D. C. Ralph, *Nat. Phys.* **13**, 300 (2017).
  - [24] S. Karube, D. Sugawara, C. Tang, T. Tanabe, Y. Oyama, and J. Nitta, *J. Magn. Magn. Mater* **516**, 167298 (2020).
  - [25] Y. Hibino, K. Hasegawa, T. Koyama, and D. Chiba, *APL Mater.* **8**, 041110 (2020).
  - [26] F. P. Chmiel, N. W. Price, R. D. Johnson, A. D. Lami, J. Schladt, G. van der Laan, D. T. Harris, J. Irwin, M. S. Rzchowski, C.-B. Eom, and P. G. Radaelli, *Nat. Mater.* **17**, 581 (2018).
  - [27] S. Karube, N. Tezuka, M. Kohda, and J. Nitta, *Phys. Rev. Appl.* **13**, 024009 (2020).

### Supplementary Material:

#### Observation of spin-splitter torque in collinear antiferromagnetic RuO<sub>2</sub>

Shutaro Karube,<sup>1,2</sup> Takahiro Tanaka,<sup>1</sup> Daichi Sugawara,<sup>1</sup>

Naohiro Kadoguchi,<sup>1</sup> Makoto Kohda<sup>1,2,3,4</sup> and Junsaku Nitta<sup>1,2,3</sup>

<sup>1</sup>Department of Materials Science, Tohoku University, Sendai 980-8579, Japan

<sup>2</sup>Center for Spintronics Research Network, Sendai 980-8577, Japan

<sup>3</sup>Center for Science and Innovation in Spintronics (Core Research Cluster), Sendai 980-8577, Japan

<sup>4</sup>Division for the Establishment of Frontier Sciences of the Organization for Advanced Studies, Sendai 980-8577, Japan

#### Out of plane crystallinity of epitaxial RuO<sub>2</sub>

We evaluated the bulk and surface crystallinities of the deposited ruthenium oxides, RuO<sub>2</sub>(100), (101), and (001), by means of conventional X-Ray Diffraction (XRD) whereby

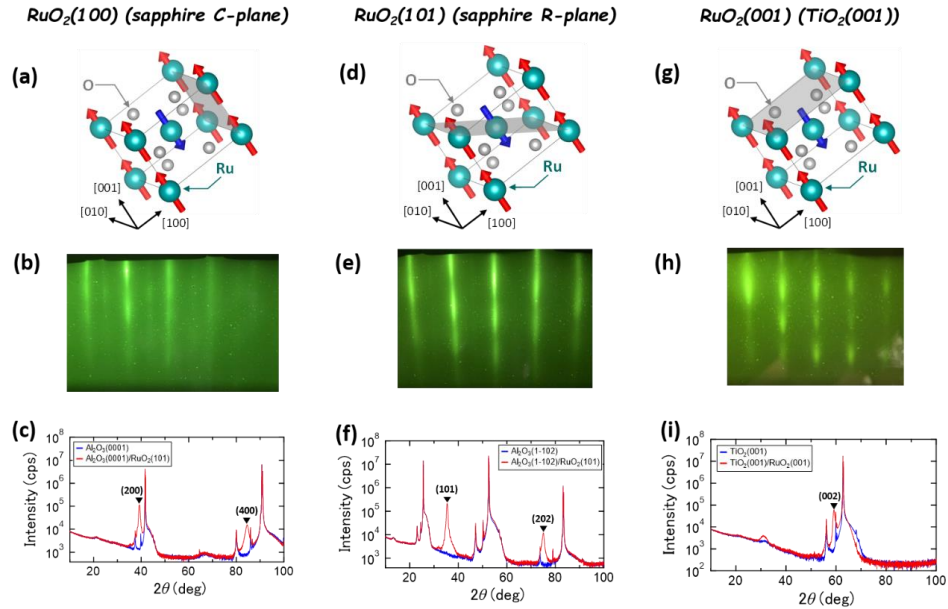


FIG. S1 (a),(d), and (g) Crystal structures and the specific crystal plane shown as a gray area with corresponding, (b),(e), and (h) RHEED patterns, and (c),(f), and (i) Out of plane XRD spectra for RuO<sub>2</sub>(100), (101) and (001), respectively. The red and blue curves only show the substrate and the deposited film onto the substrate for comparison.

the X-ray source is  $\text{CuK}\alpha$  ( $\lambda = 1.54 \text{ \AA}$ ), and Reflection High Energy Electron Diffraction (RHEED). As shown in Figs. S1(a), (d), and (g),  $\text{RuO}_2$  has a rutile-type structure (space group:  $P4_2/mnm$ ). We focused on the 3 types of  $\text{RuO}_2$ , represented by a gray plane. After deposition, we continuously investigated the surface crystallinity in-situ, and found clear streak patterns in all oxides, providing evidence of the epitaxial growth. Further the bulk crystallinities were analyzed using the XRD and found to be as single crystalline.

### Longitudinal resistivity of $\text{RuO}_2$

We measured the longitudinal resistivity of  $\text{RuO}_2(100)$ ,  $(101)$ , and  $(001)$  by means of the conventional 4-terminal method. Fig. S2 shows the dependence results on the crystal angle  $\phi_C$  for the oxides. Here, the  $\phi_C$  is the angle between the applied current direction and specific crystal direction ( $[010]$ ,  $[\bar{1}01]$ , and  $[010]$  for  $\text{RuO}_2(100)$ ,  $(101)$ , and  $(001)$ , respectively).

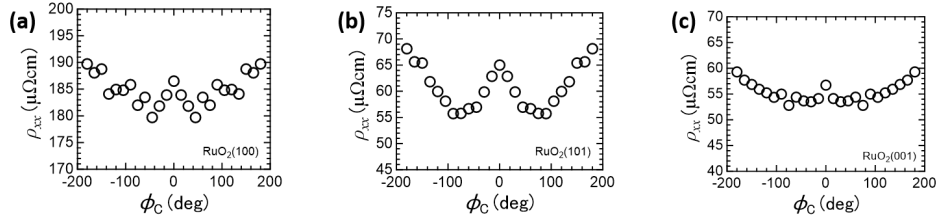


FIG. S2 Longitudinal resistivities  $\rho_{xx}$  for (a) $\text{RuO}_2(100)$ , (b) $\text{RuO}_2(101)$ , and (c) $\text{RuO}_2(001)$  as a function of the crystal angle  $\phi_C$ .

### Damping-like torque from $\text{RuO}_2$ with Cu insertion layer

We evaluated the voltage ratio regarding the damping-like (DL) torque from  $\text{RuO}_2$  in the  $\text{RuO}_2(10\text{nm})/\text{Cu}(3\text{nm})/\text{Py}(5\text{nm})$  trilayer structure to exclude the possible contribution of the exchange bias on the torque, as shown in Fig. S3. The  $\phi_C$  dependence is qualitatively the same with the case without Cu insertion shown in the main text. Note that the quantitative analysis cannot be conducted on the trilayer because the conventional analysis is only suitable for the bilayer, as shown on Eqs. (3) and (4) in the main text.



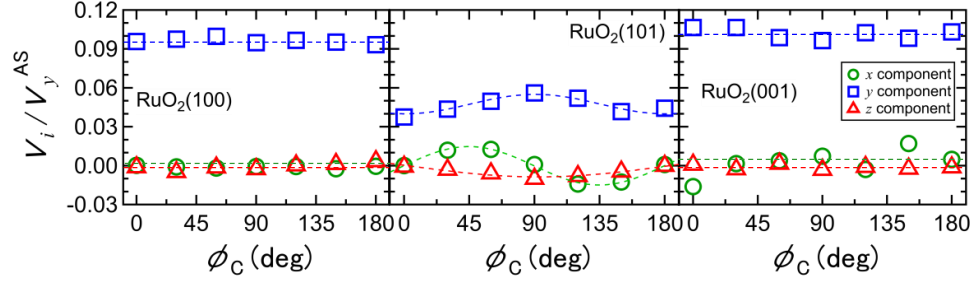


FIG. S3 The voltage ratio between  $V_i$  and the  $y$ -component of the antisymmetric part  $V_y^{\text{AS}}$  as a function of the crystal angle  $\phi_C$  for  $\text{RuO}_2(100)$ , (101), and (001). Here,  $V_i$  represents the  $V_x^S$ ,  $V_y^S$ , and  $V_z^S$  amplitudes of the  $x$ -,  $y$ - and  $z$ -components related to the DL torque, shown as a green open circle, blue open rectangle and red open triangle.

#### In-plane crystallinity of epitaxial $\text{RuO}_2(101)$

The in-plane crystallinity of the  $\text{RuO}_2(101)$  was measured as shown in Fig. S4. The 2-fold in-plane crystal symmetry is clearly observed, while the half-width is broadened. This results in a difference in the lattice constant for the rectangle planes between the  $\text{Al}_2\text{O}_3(1\bar{1}02)$  (0.48 nm and 0.89 nm) and  $\text{RuO}_2(101)$  (0.45 nm and 0.54 nm). Therefore, the distortion of the  $\text{RuO}_2$  deposited onto the  $\text{Al}_2\text{O}_3$  substrate was induced even when epitaxially grown. The report concerning the first observation of antiferromagnetism (AFM) in  $\text{RuO}_2$  [*T. Berlijn et al, Phys. Rev. Lett. 118, 077201 (2017).*] showed that this distortion is important when considering AFM order in ruthenium oxide.

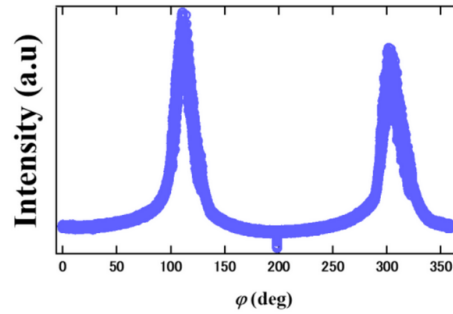


FIG. S4, In-plane crystallinity of  $\text{RuO}_2(101)$ .

**Effective perpendicular magnetic field  
induced by z-polarized spin current from RuO<sub>2</sub>(101)**

We successfully demonstrated field-free switching in the Co layer using the z-component of the DL torque generated from RuO<sub>2</sub>(101) when a charge current along [010] direction ( $\phi_C = 90$  deg). To ensure that switching is generated by the z-component, we analyzed the effective perpendicular magnetic field induced by the component in a measurement of the anomalous Hall effect when applying an external magnetic field. When we apply a low-amplitude current, such as  $\pm 10$  mA, the switching behavior is very similar and is independent of current. Alternatively, applying a higher amplitude current, such as  $\pm 26$  mA, the hysteresis curve was highly varied by the current.

This is attributed to the effective perpendicular magnetic field  $\mu_0 H_z^{\text{eff}}$ , induced by the z-component of the DL torque from the RuO<sub>2</sub>. Here, we define the effective field  $\mu_0 H_z^{\text{eff}} = -\mu_0(H_+ + H_-)/2$ , as shown in Fig. S5 (a), where  $H_+$  and  $H_-$  are the switching fields for the Co layer. The effective field depends on the applied current amplitude shown in Fig. S5(b), meaning that it is attributed to the z-polarized spin current via the spin-splitter effect.

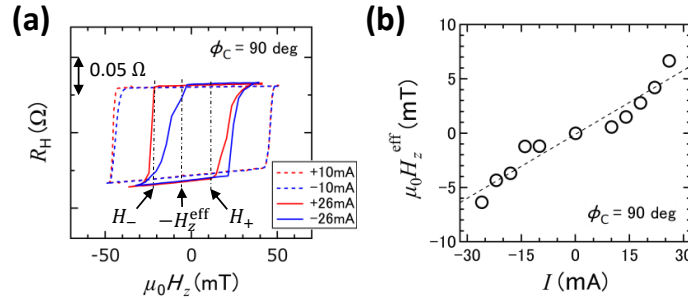


FIG. S5 (a) Hall resistance as a function of the perpendicular magnetic field  $\mu_0 H_z$  when applying the charge current along [010] direction ( $\phi_C = 90$  deg). The Hall resistance at  $\pm 10$  mA does not depend on the current, whereas the resistance at  $\pm 26$  mA is clearly determined by the presence and large amplitude of the applied current. (b) Effective z-polarized magnetic field, extracted from the definition in the manuscript, depending on the current amplitude in the case of [010] direction.

**Perpendicular exchange bias on the Co layer from the antiferromagnetic RuO<sub>2</sub>**

The conventional anomalous Hall resistances of the Co layer for the switching experiment were measured with an applied perpendicular magnetic field for  $\phi_C = 0$ , and  $90$  deg, shown in Fig. S6. The perpendicular exchange bias  $\mu_0 H_z^{\text{EB}}$  was only found when  $\phi_C = 0$  deg and at approximately  $10$  mT. Alternatively, the exchange bias is negligible when  $\phi_C = 90$  deg, in which full switching was observed. Therefore, we concluded that the exchange bias does not

contribute to the field-free switching in this case as shown in the main text. On the other hand, the finite exchange bias, when  $\phi_C = 0$  deg, interferes with the switching of the Co magnetization, as shown in Fig. 4(b) in the main text. In particular, there is no  $z$ -component of the DL torque in the  $\phi_C = 0$  deg case. Thus, halfway switching was seen in the experiment with a multi-domain state.

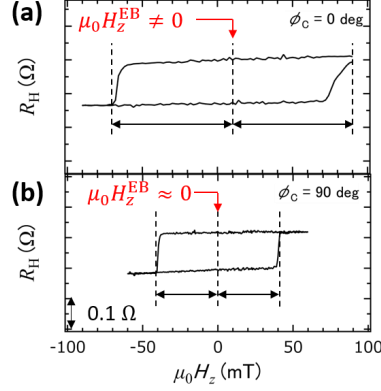


FIG. S6 Hall resistances when applying a perpendicular magnetic field in the case of (a)  $\phi_C = 0$  deg, (b)  $\phi_C = 90$  deg.

### Current shunting into Pt layer

Regarding the field-free switching measurement, we calculated the current shunting factors  $\xi_{\text{Pt}}$ ,  $\xi_{\text{RuO}_2}$  for both the Pt and RuO<sub>2</sub> layers using each resistivity  $\rho_i$  and thickness  $t_i$  ( $i = \text{Pt}$  or RuO<sub>2</sub>), based on the equations below. Here, the much thinner Ru and Co layers were assumed to not contribute to the electrical conduction due to much higher resistivities than those of the Pt and RuO<sub>2</sub> layers.

$$\xi_{\text{Pt}} = \frac{1}{1 + \frac{\rho_{\text{Pt}} t_{\text{RuO}_2}}{t_{\text{Pt}} \rho_{\text{RuO}_2}}} = 0.06$$

$$\xi_{\text{RuO}_2} = \frac{1}{1 + \frac{\rho_{\text{RuO}_2} t_{\text{Pt}}}{t_{\text{RuO}_2} \rho_{\text{Pt}}}} = 0.94$$

We determined and used the following parameter values:  $t_{\text{Pt}} = 2$  nm,  $t_{\text{RuO}_2} = 10$  nm,  $\rho_{\text{Pt}} = 160$   $\mu\Omega\text{cm}$ ,  $\rho_{\text{RuO}_2} = 55$   $\mu\Omega\text{cm}$ . Note that the high resistivity of the 2 nm-thick Pt layer originated from surface scattering [*K. Fuchs, Proc. Cambridge Phil. Soc.* **34**, 100 (1938) and

*E. H. Sondheimer, Advan. Phys. 1, 1 (1952)*]. The shunting factor of the RuO<sub>2</sub> layer is much higher than that of the Pt layer; therefore, we can neglect contributions such as current shunting into and spin-orbit torque from the Pt layer in the switching measurement.